Inorg. Chem. **2004**, *43*, 4579–4589

Determination by X-ray Absorption Spectroscopy of the Fe–Fe Separation in the Oxidized Form of the Hydroxylase of Methane Monooxygenase Alone and in the Presence of MMOD

Deanne Jackson Rudd,[†] Matthew H. Sazinsky,[‡] Maarten Merkx,[‡] Stephen J. Lippard,[‡] Britt Hedman,*[,§] and Keith O. Hodgson*[,†,§]

Departments of Chemistry, Stanford University, Stanford, California 94305 and Massachusetts Institute of Technology, Cambridge, Massachusetts 02139, and Stanford Synchrotron Radiation Laboratory, Stanford University, Stanford, California 94309

Received March 4, 2004

The diiron active site in the hydroxylase of *Methylococcus capsulatus* (Bath) methane monooxygenase (MMOH) has been studied in the oxidized form by X-ray absorption spectroscopy (XAS). Previous investigations by XAS and X-ray crystallography have identified two different distances (3.0 and 3.4 Å) between the two Fe atoms in the dinuclear site. The present study has employed a systematic extended X-ray absorption fine structure (EXAFS) fitting methodology, utilizing known and simulated active site and relevant model structures, to determine unambiguously the Fe–Fe separation in the oxidized form of MMOH. Consistent and unique fits were only possible for an Fe–Fe distance of 3.0 Å. This methodology was then applied to study potential changes in the active site local structure in the presence of MMOD, a protein of unknown function in multicomponent MMO. Fe K-edge and EXAFS analyses revealed negligible changes in the diiron site electronic and geometric structure upon addition of MMOD to oxidized MMOH.

Introduction

Metalloenzymes employed by methanotrophic bacteria catalyze the conversion of methane to methanol (eq 1), an important step in the carbon cycle. All methanotrophs express a membrane-bound copper-containing enzyme called particulate methane monooxygenase (pMMO), which catalyzes this reaction. In the absence of copper, however, some methanotrophs, such as *Methylococcus capsulatus* (Bath) and *Methylosinus trichosporium* OB3b, express a soluble iron-containing methane monooxygenase (sMMO) to perform the same function.[1]

$$CH_4 + O_2 + NADH + H^+ \rightarrow CH_3OH + H_2O + NAD^+ \quad (1)$$

The protein system of sMMO comprises four components. The $\alpha_2\beta_2\gamma_2$ hydroxylase (MMOH) contains a bridged non-heme diiron site in each α-subunit where dioxygen activation and methane hydroxylation occur. The [2Fe−2S]-containing reductase (MMOR) shuttles electrons from NADH to MMOH. The cofactorless protein MMOB serves a regulatory role by altering the diiron site and is required for activity. The fourth component, MMOD, is of unknown function but binds to the hydroxylase and inhibits activity. The catalytic cycle starts with MMOH in the Fe(III)Fe(III) resting state. MMOR then docks to MMOH and transfers two electrons to the diiron centers from NADH. MMOH, now in the active Fe(II)Fe(II) state, reacts with O_2 in the presence of MMOB to produce a series of intermediates and ultimately hydroxylates methane.[1]

Several structural studies have detailed the active site of MMOH in the oxidized (H_{ox}), reduced (H_{red}), and mixed-valent (H_{mv}) oxidation states.[2−12] Extended X-ray absorption

* Authors to whom correspondence should be addressed. E-mail: hodgson@ssrl.slac.stanford.edu (K.O.H.); hedman@ssrl.slac.stanford.edu (B.H.).
[†] Department of Chemistry, Stanford University.
[‡] Massachusetts Institute of Technology.
[§] Stanford Synchrotron Radiation Laboratory, Stanford University.

(1) Merkx, M.; Kopp, D. A.; Sazinsky, M. H.; Blazyk, J. L.; Müller, J.; Lippard, S. J. *Angew. Chem., Int. Ed.* **2001**, *40*, 2782−2807.
(2) Prince, R. C.; George, G. N.; Savas, J. C.; Cramer, S. P.; Patel, R. N. *Biochim. Biophys. Acta* **1988**, *952*, 220−229.
(3) DeWitt, J.; Hedman, B.; Ericson, A.; Hodgson, K. O.; Bentsen, J.; Beer, R.; Lippard, S. J.; Green, J.; Dalton, H. *Physica B* **1989**, *158*, 97−98.
(4) DeWitt, J. G.; Bentsen, J. G.; Rosenzweig, A. C.; Hedman, B.; Green, J.; Pilkington, S.; Papaefthymiou, G. C.; Dalton, H.; Hodgson, K. O.; Lippard, S. J. *J. Am. Chem. Soc.* **1991**, *113*, 9219−9235.

10.1021/ic049716b CCC: $27.50
Published on Web 06/23/2004

fine structure (EXAFS) and crystallographic investigations of H_{ox} determined that each Fe center in H_{ox} is ligated in a pseudo-octahedral arrangement and that the 2 Fe atoms are typically bridged by 1 glutamate and 2 O-atom bridges that are assigned as OH^- or $H_3O_2^-$, rather than oxo, units. One Fe center is coordinated by 1 histidine, 1 glutamate, and 1 water, in addition to the 3 bridging ligands, while the second Fe has an additional glutamate ligand instead of the water.

Despite this wealth of structural information, which represents the fruit of more than 10 years of research, there is still ambiguity regarding the Fe−Fe separation in H_{ox} as determined by EXAFS methodologies. Original EXAFS studies performed on H_{ox} from *M. capsulatus* (Bath) in 1991 concluded that the distance between the Fe pair was 3.4 Å, with nearly equally strong evidence for a shorter distance of 3.0 Å.[4] The empirical fitting method used at that time extracted amplitude and phase fitting parameters from experimental data of model complexes that were considered reasonable mimics of the active site structure. The two models used in this study differed in their bridging modes. The first model was an oxo-bridged diiron complex with an Fe−Fe separation of 3.16 Å, whereas a hydroxo-bridged species with an Fe−Fe separation of 3.44 Å was chosen as the second model. Both model complexes afforded Fe−Fe vectors that provided reasonable fits to the Fourier filtered second shell data, resulting in two minima with Fe−Fe separations of 3.0 and 3.4 Å, respectively. Due to a slightly lower fit error and stronger resemblance of the EXAFS data modulation, the longer distance was accepted as being the observed Fe−Fe separation. This conclusion was supported by the absence of signature features in the EXAFS and pre-edge data for an oxo-bridged center, which would have a shorter Fe−Fe distance. Furthermore, EPR spectroscopy indicated weak antiferromagnetic exchange, consistent with OH^- rather than O^{2-} bridging. The authors indicated concern regarding the model bias in their fitting protocol, however, and cautioned that this bias could have important implications when determining metal−metal separations by EXAFS.

Further EXAFS and crystallography studies in recent years have not definitively eliminated the initial doubt exhibited by this first EXAFS study with regard to the Fe−Fe separation. The timeline in Figure 1 illustrates the number of structural studies performed on H_{ox} and the Fe−Fe separations that were found in each case. There are clearly two distances indicated from the EXAFS studies: 3.0 and 3.4 Å. The earliest crystallographic study revealed the longer Fe−Fe separation attributed to the presence of acetate rather than a single-atom bridge in the active site pocket. More recent studies found shorter distances, owing to the presence of a single-atom bridge. In addition, there can be a 0.1−0.2 Å error associated with distances in protein crystal structures, depending on the resolution of the structure and many other factors.[13] For EXAFS, which is excellent at determining local-structure distances between atoms (errors on the order of 0.01−0.03 Å),[14] recent approaches that allow accurate ab initio calculation of the phase and amplitude functions, coupled with enhancement in beam lines and instrumentation, have led to improvements in approaches to the study of complex systems. Given the structural history and the improved XAS tools, a systematic and thorough EXAFS investigation of the active site of H_{ox} has been undertaken.

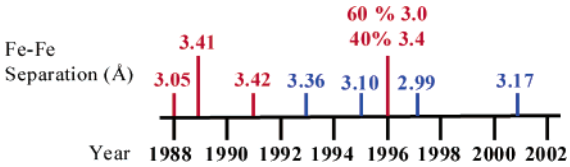

Figure 1. Time line depicting structural determinations of the Fe−Fe separation in H_{ox} from 1988 to 2002. Red indicates EXAFS studies. Blue indicates protein crystal diffraction studies.[2−6,8,10,11]

This study probes in particular both the appropriateness of starting models for theoretical calculation of phase and amplitude functions and the protocol applied to fit the experimental protein data. In addition to determining the solution active-site structure of H_{ox}, there is continued interest in understanding how other protein components and substrates interact with the diiron site of MMOH and how they might modulate the structure. The initial unmodified structure must therefore be unambiguously known.[7,9,12,15] MMOD affects the optical spectrum of H_{ox}.[16] Features typical of oxo-bridged diiron(III) clusters appear in the optical spectrum of H_{ox} when MMOD is present. The extinction coefficients for these new features are low compared to synthetic oxo-bridged diiron(III) complexes, however, suggesting that MMOD may only produce this effect in a small percentage of the H_{ox} molecules.[16] Kinetic data reveal that MMOD binds to MMOH with similar affinity to that of MMOB or MMOR,[16] but a crystal structure of the protein components in the complex has thus far been elusive. Therefore, this study also employs XAS K-edges and EXAFS to investigate the electronic and geometric structure of H_{ox} in the presence of MMOD, and compares the results to a firmly established base structure of H_{ox}.

Experimental Section

A. Protein Preparation. MMOH and MMOD were purified as previously described.[16,17] The purified hydroxylase contained 3.9

(5) Rosenzweig, A. C.; Frederick, C. A.; Lippard, S. J.; Nordlund, P. *Nature* **1993**, *366*, 537−543.
(6) Rosenzweig, A. C.; Nordlund, P.; Takahara, P. M.; Frederick, C. A.; Lippard, S. J. *Chem. Biol.* **1995**, *2*, 409−418.
(7) DeWitt, J. G.; Rosenzweig, A. C.; Salifoglou, A.; Hedman, B.; Lippard, S. J.; Hodgson, K. O. *Inorg. Chem.* **1995**, *34*, 2505−2515.
(8) Shu, L.; Liu, Y.; Lipscomb, J. D.; Que, L., Jr. *J. Biol. Inorg. Chem.* **1996**, *1*, 297−304.
(9) Rosenzweig, A. C.; Brandstetter, H.; Whittington, D. A.; Nordlund, P.; Lippard, S. J.; Frederick, C. A. *Proteins: Struct., Funct., Genet.* **1997**, *29*, 141−152.
(10) Elango, N.; Radhakrishnan, R.; Froland, W. A.; Waller, B. J.; Earhart, C. A.; Lipscomb, J. D.; Ohlendorf, D. H. *Protein Sci.* **1997**, *6*, 556−568.
(11) Whittington, D. A.; Lippard, S. J. *J. Am. Chem. Soc.* **2001**, *123*, 827−838.
(12) Whittington, D. A.; Sazinsky, M. H.; Lippard, S. J. *J. Am. Chem. Soc.* **2001**, *123*, 1794−1795.
(13) Freeman, H. C. In *Spectroscopic Methods in Bioinorganic Chemistry*; Solomon, E. I., Hodgson, K. O., Eds.; American Chemical Society: Washington, DC, 1998; pp 62−95.
(14) Cramer, S. P.; Hodgson, K. O. *Prog. Inorg. Chem.* **1979**, *25*, 1−39.
(15) Davydov, R.; Valentine, A. M.; Komar-Panicucci, S.; Hoffman, B. M.; Lippard, S. J. *Biochemistry* **1999**, *38*, 4188−4197.
(16) Merkx, M.; Lippard, S. J. *J. Biol. Chem.* **2002**, *277*, 5858−5865.

Fe/heterodimer and had an activity between 250 and 300 nmol/min/mg for polypropylene at 25 °C. XAS samples contained 500 μM MMOH ± 1000 μM MMOD dissolved in 25 mM MOPS, pH 7.0 and 25% glycerol. For each sample, ~100 μL of sample solution was transferred into a Lucite XAS cell with 37 μm Kapton tape windows and immediately frozen in liquid nitrogen.

B. Data Collection and Reduction. The X-ray absorption spectra for the MMOH samples were measured at the Stanford Synchrotron Radiation Laboratory (SSRL) on unfocused 8-pole wiggler beam line 7-3, with the ring operating at 3 GeV, 50−100 mA. A Si(220) monochromator was utilized for energy selection at the Fe K-edge. The monochromator was detuned 50% at 7987 eV to minimize higher harmonic components in the X-ray beam. The sample was maintained at 10 K during data collection using an Oxford Instruments CF1208 continuous flow liquid helium cryostat. Data were measured to $k = 15$ Å^{-1} in fluorescence mode by using a Canberra Ge 30-element array detector. Internal energy calibration was performed by simultaneous measurement of the absorption of an Fe foil placed between two ionization chambers located after the sample. The first inflection point of the foil was assigned to 7111.2 eV.

The oxidized MMOH samples were monitored for photoreduction throughout the course of data collection. A gradual decrease in the energy of the edge region is indicative of reduction from Fe^{III} to Fe^{II}. After 5 scans, the edge region was shifted by ~0.5 eV. Two distinct and physically separate spots on the sample were exposed. Analysis of the EXAFS showed only a very small effect from such photoreduction. Successive two-scan averages through the fifth scan from each of the two spots resulted in very minor differences in the EXAFS at high *k*. Therefore, it was determined that the first five scans from each spot could be included in the final average. This procedure resulted in a 10-scan average for the oxidized MMOH sample. The oxidized MMOH + MMOD sample appeared to photoreduce slightly faster than the oxidized MMOH sample (after 4 scans, the edge region was shifted by ~0.8 eV). Again, the EXAFS region was less affected by the photoreduction and two-scan averages of the first and second, and of the third and fourth, scans were compared for each spot. Very minor differences were observed in these two scan averages at high *k*. Therefore, it was determined that the first 4 scans from each of 4 spots would be included in the final average. This protocol resulted in a 16-scan average for the oxidized MMOH + MMOD sample.

The averaged data were processed by fitting a second-order polynomial to the post-edge region and subtracting this background from the entire spectrum. A three-region spline of orders 2, 3, and 3 was used to model the smooth background above the edge. Normalization of the data was achieved by subtracting the spline and setting the edge jump to 1.0 in the post-edge region. The resultant EXAFS was k^3-weighted to enhance the impact of high-*k* data. Because of the signal-to-noise level, the EXAFS data were truncated at $k = 13$ Å^{-1} during the analysis.

Data Analysis

A. Model Construction. Information from previous EXAFS studies of H_{ox} indicated the Fe−Fe wave vector to be very sensitive to the model used to extract fitting parameters.[4] Although the method used here directly calculates the phase and amplitude functions,[18−21] rather than extracting these parameters from experimental model complex data, the calculations still rely on an initial structural model. To ensure that the fit was not biased to this initial model, and in particular to the initial Fe−Fe separation, several models were created having a range of Fe−Fe separations. The most recent crystal structure of H_{ox} (1.96 Å resolution, Fe−Fe separation of 3.17 Å) provided an excellent starting point.[11] A total of 15 systematically constructed variations of this structure were produced with Fe−Fe separations ranging from 2.8 to 3.5 Å, in 0.05 Å steps. The angles between the Fe atoms and bridging ligands were allowed to contract or expand to accommodate the variable Fe−Fe distance, which kept the Fe−ligand distances constant. Phase and amplitude functions were calculated from each structure variant and used to fit the experimental EXAFS data of H_{ox}.

In many EXAFS studies, the investigators are not so fortunate as to have a crystal structure of the protein to use as their input model for calculation of phase and amplitude functions. In these cases, Cartesian coordinates from crystal structures of small, synthetic complexes that are assumed to approximate the bonding in the protein active site are often used. This approach is more analogous to the empirical fitting method described previously, except that it is unnecessary to collect EXAFS data on each model complex because the phase and amplitude functions are calculated directly from the known structures. Although there are disadvantages to using this approach (vide infra), these known complexes provide functions that are chemically reasonable and give insight into the types of bonding and interatomic distances that are possible. To extend the investigation into the model bias surrounding the EXAFS fits to H_{ox}, 11 diiron(III) model complexes were chosen from the Cambridge Structural Database[22] with Fe−Fe separations of 2.9−3.5 Å.[23−32] Phase and amplitude functions were calculated directly from their Cartesian coordinates and used to fit the experimental EXAFS data of H_{ox}.

(17) Gassner, G. T.; Lippard, S. J. *Biochemistry* **1999**, *38*, 12768−12785.
(18) Rehr, J. J.; Mustre de Leon, J.; Zabinsky, S. I.; Albers, R. C. *J. Am. Chem. Soc.* **1991**, *113*, 5135−5140.
(19) Mustre de Leon, J.; Rehr, J. J.; Zabinsky, S. I.; Albers, R. C. *Phys. Rev. B* **1991**, *44*, 4146−4156.
(20) Zabinsky, S. I.; Rehr, J. J.; Ankudinov, A.; Albers, R. C.; Eller, M. J. *Phys. Rev. B* **1995**, *52*, 2995−3009.
(21) Rehr, J. J.; Albers, R. C. *Rev. Mod. Phys.* **2000**, *72*, 621−654.
(22) *Cambridge Structural Database*; Cambridge University: Cambridge, England, 2003.
(23) Zheng, H.; Zang, Y.; Dong, Y.; Young, V. G., Jr.; Que, L., Jr. *J. Am. Chem. Soc.* **1999**, *121*, 2226−2235.
(24) O'Brien, R. J.; Richardson, J. F.; Buchanan, R. M. *Acta Crystallogr., Sect. C* **1991**, *47*, 2307−2310.
(25) Oberhausen, K. J.; Richardson, J. F.; O'Brien, R. J.; Buchanan, R. M.; McCusker, J. K.; Webb, R. J.; Hendrickson, D. N. *Inorg. Chem.* **1992**, *31*, 1123−1125.
(26) Armstrong, W. H.; Lippard, S. J. *J. Am. Chem. Soc.* **1983**, *105*, 4837−4838.
(27) Norman, R. E.; Holz, R. C.; Ménage, S.; O'Connor, C. J.; Zhang, J. H.; Que, L., Jr. *Inorg. Chem.* **1990**, *29*, 4629−4637.
(28) Spek, A. L.; Bouwman, E.; Haasnoot, J. G.; Reedijk, J. Bijvoet Center for Biomolecular Research, Department of Crystal and Structural Chemistry, Utrecht University, The Netherlands, Private Communication to the Cambridge Structural Database, 2001.
(29) Umakoshi, K.; Tsuruma, Y.; Oh, C.-E.; Takasawa, A.; Yasukawa, H.; Sasaki, Y. *Bull. Chem. Soc. Jpn.* **1999**, *72*, 433−440.
(30) Wilkinson, E. C.; Dong, Y.; Que, L., Jr. *J. Am. Chem. Soc.* **1994**, *116*, 8394−8395.
(31) Turowski, P. N.; Armstrong, W. H.; Liu, S.; Brown, S. N.; Lippard, S. J. *Inorg. Chem.* **1994**, *33*, 636−645.
(32) Neves, A.; de Brito, M. A.; Vencato, I.; Drago, V.; Griesar, K.; Haase, W.; Mascarenhas, Y. P. *Inorg. Chim. Acta* **1993**, *214*, 5−8.

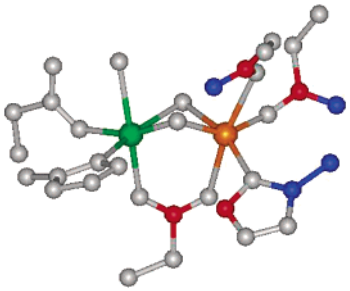

Figure 2. The active site of H_{ox}. To illustrate types of second shell scattering, absorbing Fe is shown in orange, C ~3.0 Å from Fe is shown in red, Fe scatterer is shown in green, and C/O ~3.4 Å from Fe is shown in blue. (Adapted from ref 11.)

B. Calculation of Functions and EXAFS Fitting. Theoretical EXAFS signals $\chi(k)$ were calculated using FEFF (version 7.02)[18−21] and fit to the data with EXAFSPAK.[33] The experimental energy threshold, E_0 (the point at which $k = 0$), was chosen as 7130 eV and was allowed to vary by a common amount (ΔE_0) for all components within a given fit. The structural parameters that were varied during the refinements include the bond distance (R) and the bond variance (σ^2). The σ^2 parameter is related to the Debye−Waller factor, which is a measure of thermal vibration and static disorder of the absorbers and scatterers. Coordination numbers were systematically varied during the course of the analysis but were not allowed to vary within a given fit. Although the Fourier transforms of the EXAFS data were often used to evaluate the quality of the fit, the fits were performed on the k^3 EXAFS data in k-space.

The Fourier transform of H_{ox} displays a strong second shell peak centered at ~3.0 Å. Attempts to fit this peak solely with Fe−Fe backscattering waves were unsuccessful. Similarly, Fe−C backscattering waves representing different Fe−C distances could not satisfactorily fit this peak. Fits were also performed in which two distinct Fe−Fe vectors were included, with distances of ~3.0 and ~3.4 Å and varying coordination numbers totaling 1. All such fits, irrespective of which light atom paths were included, and those in which no light atom scattering contribution was used between 2.6 and 4.0 Å, resulted in unreasonable R or σ^2 values. It is therefore concluded that the peak is a consequence of a combination of light atom−Fe and Fe−Fe backscattering at a single distance. Three types of scatterers were identified as possible contributors to this peak: carbon atoms 2 bonds away from Fe at ~3.0 Å, Fe (assumed to be between 2.8 and 3.5 Å away from the other Fe), and carbon or oxygen atoms 2 or 3 bonds away from Fe at ~3.4 Å (see Figure 2). Both single and multiple scattering from the possible light atom contributors were considered. Three different types of fits were developed on the basis of these possible scatterers: type 1 included C at ~3.0 Å and Fe of variable distance; type 2 included C/O at ~3.4 Å and Fe of variable distance; and type 3 included C at ~3.0 Å, C/O at ~3.4 Å, and Fe of variable distance. Each fit contained the same first shell and long-distance multiple scattering contributions.

C. Pre-Edge Analysis. The energies and intensities of the pre-edge transitions were determined by least-squares fits to the data using EDG_FIT.[33] Pseudo-Voigt line shapes (sums of Lorentzian and Gaussian functions) were used to model the pre-edge features. The amplitude, energy position, and full width at half-maximum (fwhm) were varied for each peak during the fitting procedure. A wide transition was used as a rising edge background and was considered acceptable as long as it remained lower in intensity than the white line maximum of the edge. The data and the second derivative of the data were fit simultaneously, and both needed to be well fit within the noise of the data for the fit to be acceptable. All data were fit over 3 energy ranges, 7108−7116, 7108−7117, and 7108−7118 eV, and 3 fits were performed for each range, for a total of 9 fits for each complex. The first fit allowed the background and transition parameters (amplitude, position, and fwhm) to float freely to obtain the best fit. The two subsequent fits kept the fwhm of the background peak fixed to a value ±0.5 from the original value and allowed all other parameters to float. The values reported for the energy position and intensity, calculated as amplitude multiplied by fwhm, of each transition are the average for all successful fits, and the error is the standard deviation for that value over all successful fits.[34]

Results

A. Paths Calculated from Protein Crystal Structure Variations. Three types of EXAFS fits (types 1, 2, and 3) were tested for each of 15 crystal structure variations, and the results are summarized in Table 1. Similar fits with different initial Fe−Fe separations have been grouped for simplicity. The fit values given are for one particular fit within the group but are representative of all fits of that class. All fits include a split first shell with 5 O/N at 1.99 Å and 1 O at 2.45 Å. The σ^2 value for the 1.99 Å O path is relatively high for a first shell wave but is reasonable since it represents the average first shell environment of 4 Fe atoms (2 Fe in each of 2 protomers). Attempts were made to split this shell into two paths, but this procedure did not improve the fit significantly. There was no evidence for a short (~1.8 Å) O contribution typical of an oxo-bridge between the two Fe centers. This finding supports previous studies[4,8,11] and confirms that H_{ox} contains a OH^-- or $H_3O_2^-$-bridged binuclear site. The O path that fit to a distance of 2.45 Å agrees well with the crystal structure of H_{ox}, which indicates that at least one O ligand to each Fe was at a distance ≥ 2.4 Å.[11] This longer first shell scatterer may represent a long terminal water ligand or a weak OH^- or $H_3O_2^-$ bridge between the two Fe atoms.

The second shell contained possible contributions from 5 sources: C ~3.0 Å from Fe (**PathC^s**) and the corresponding multiple scattering, Fe (**PathFe**), and C/O ~3.4 Å from Fe

(33) George, G. N. *EXAFSPAK & EDG_FIT*; Stanford Synchrotron Radiation Laboratory, Stanford Linear Accelerator Center, Stanford University: Stanford, CA, 2000.

(34) Westre, T. E.; Kennepohl, P.; DeWitt, J. G.; Hedman, B.; Hodgson, K. O.; Solomon, E. I. *J. Am. Chem. Soc.* **1997**, *119*, 6297−6314.

Table 1. Results of Second Shell Fits[a] to H_{ox} Using Protein Crystal Structure Variations as Input Models

	type 1[b]				type 2[b]				type 3[b]			
	R (Å)	σ^2 (Å^2)	ΔE_0	*F*[c]	*R* (Å)	σ^2 (Å^2)	ΔE_0	*F*[c]	*R* (Å)	σ^2 (Å^2)	ΔE_0	*F*[c]
initial Fe−Fe (Å)		2.80−2.90, 3.20[d]				2.80−3.25[d]				2.80−2.90[d]		
4C	3.06	0.0003	−0.38	0.34			−1.82	0.22	3.03	0.0015	−1.48	0.21
1Fe	2.95	0.0113			3.03	0.0033			2.73	0.0183		
4C/O					3.40	0.0038			3.37	0.0016		
4C/O−N/C					3.56	0.0051			3.42	0.0023		
initial Fe−Fe (Å)		2.95−3.10[d]				3.30−3.50[d]				2.95, 3.15, 3.20, 3.35, 3.45[d]		
4C	3.25	0.1730	−0.80	0.31			−5.29	0.36	3.03	0.0003	−1.95	0.21
1Fe	3.03	0.0029			3.30	−0.0022			3.17	0.0072		
4C/O					3.43	−0.0032			3.37	0.0021		
4C/O−N/C					3.56	0.0063			3.35	0.0033		
initial Fe−Fe (Å)		3.15, 3.25−3.45[d]								3.00−3.10[d]		
4C	3.04	0.0008	−1.41	0.33					3.01	0.0689	−2.43	0.22
1Fe	3.40	0.0082							3.02	0.0038		
4C/O									3.38	0.0037		
4C/O−N/C									3.51	0.0120		

[a] Each fit also included 2 first shell O/N paths (at 1.99 and 2.45 Å) and 1 long-distance multiple scattering path (at ∼4.3 Å) to complete the fit. [b] Fits of type 1 included contributions from C ∼3.0 Å from Fe (**PathC^s**) and Fe (**PathFe**). Fits of type 2 included contributions from C/O ∼3.4 Å from Fe (**PathC$^l_{ss}$**), the corresponding multiple scattering (**PathC$^l_{ms}$**), and Fe (**PathFe**). Fits of type 3 included all 4 paths (**PathC^s**, **PathFe**, **PathC$^l_{ss}$**, and **PathC$^l_{ms}$**). [c] Error (*F*) is defined as $F = \sum[[(\chi_{obsd} - \chi_{calcd})^2 k^6]/n]$ where *n* is the number of data points. [d] Each starting distance provided fits that, within error, could be grouped together. The fit values shown are from one fit but are representative of all fits of that group.

(**PathC$^l_{ss}$**) and the corresponding multiple scattering (**PathC$^l_{ms}$**). Inclusion of multiple scattering involving the shorter distance C atoms did not reduce the fit error for any of the fits and was therefore not used. This result is not surprising since the largest C−O/N−Fe angle for any of these paths is 136°, according to the crystal structure.[11] Conversely, the multiple scattering contribution of the C/O atoms ∼3.4 Å from Fe was necessary to provide good fits to the data. This result was unexpected given that the C/O−N/C−Fe angles for these paths were not much larger, and in some cases smaller, than those for the shorter C path, according to the crystal structure.[11] However, **PathC^l** and **PathC$^l_{ms}$** combined to improve the fit significantly to the high *R* side of the second shell peak (vide infra). Both paths were therefore included in type 2 and type 3 fits.

Also included in all fits was a multiple scattering contribution at 4.32 Å representing the average scattering from N and C atoms 3 bonds from Fe. This multiple scattering path is very strong in amplitude despite its distance from Fe due to the large N/C−N/C−Fe angles (150−170°). Thus, the wave contributes significantly to the Fourier transform between $R = 3-4$ Å.

Type 1 Fits. Fits of type 1 included **PathC^s** and **PathFe** only and resulted in 3 classes of fits. Initial Fe−Fe separations of 2.80−2.90 and 3.20 Å gave the fit shown in Figure 3a, with **PathC^s** and **PathFe** fitting to 3.06 and 2.95 Å, respectively. **PathC^s** was dominant, whereas **PathFe** had a very high σ^2 value. It was clear from this first class of fits that **PathC^s** and **PathFe** were highly correlated in fitting the second shell. When the initial Fe−Fe separation was lengthened to between 2.95 and 3.10 Å, **PathC^s** and **PathFe** were again correlated, but in this class, **PathFe** was the dominant contributor at 3.03 Å, whereas **PathC^s** fit to 3.25 Å, with an extremely high σ^2 value (Figure 3b). Visual inspection of the two classes of fits revealed that the agreement between the Fourier transforms of the data and the fit depended strongly on whether C or Fe dominated the fit. The latter provided much better overall agreement, especially in the $R = 2.0-2.5$ Å region, but less so in the higher-*R* region, between $R = 2.5-3.5$ Å, where noticeable intensity was lacking.

An interesting class of fits resulted when the initial Fe−Fe separation was lengthened to between 3.25 and 3.45 Å for type 1 fits. **PathC^s** fit to a distance of 3.04 Å (with a very low σ^2 value) and **PathFe** to a distance of 3.40 Å. This value is the same Fe−Fe separation reported in previous EXAFS studies of H_{ox}.[4] Inspection of Figure 3c indicated, however, that this combination of paths was not correct because the fit provided too much intensity to the high *R* side of the second shell peak, while **PathC^s** required a very low σ^2 value to fit the low *R* side. It was concluded that none of the type 1 fits provided an adequate fit to the data.

Type 2 Fits. PathFe, **PathC$^l_{ss}$**, and **PathC$^l_{ms}$** were included in type 2 fits, which divided themselves into two distinct classes dependent upon the initial Fe−Fe separations, 2.80−3.25 and 3.30−3.50 Å, respectively. The first class resulted in an excellent fit to the data (Figure 4a), with **PathFe** at a distance of 3.03 Å, **PathC$^l_{ss}$** at 3.40 Å, and **PathC$^l_{ms}$** at 3.56 Å, all with reasonable σ^2 values. The fit error was low, and all features of the Fourier transform were well modeled. **PathC$^l_{ss}$** and **PathC$^l_{ms}$** interfered destructively, as can be seen in the EXAFS deconvolution in the inset of Figure 4a. Their combined effect allowed a shoulder at $k \approx 8$ Å^{-1} to have an improved fit, however, as compared to the fit shown in Figure 3b, and the *R* and σ^2 values are chemically reasonable.

When the initial Fe−Fe separation was lengthened beyond 3.25 Å, the fit shown in Figure 4b resulted. The initial distance between the two Fe atoms was large enough that the least-squares fitting procedure would not reduce this distance to below 3.3 Å. In addition, the σ^2 values for **PathFe** and **PathC$^l_{ss}$** were negative, and therefore unrealistic. Because there was no path included in this type of fit that could add to the low *R* side of the peak, it remained poorly

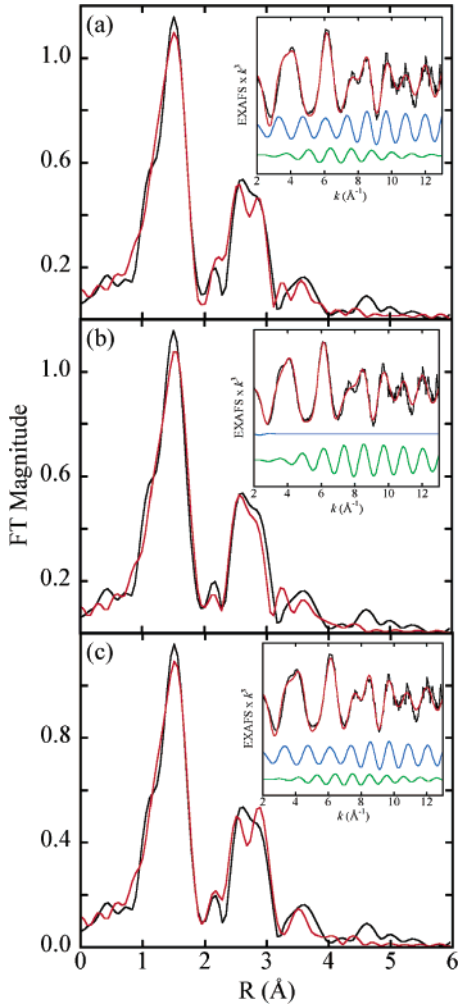

Figure 3. Nonphase shift corrected Fourier transforms (black) and fits of type 1 to the data (red) for H_{ox} with initial Fe−Fe separations from protein crystal structure variations of (a) 2.80−2.90, (b) 2.95−3.10, and (c) 3.15−3.45 Å. Insets show EXAFS data of H_{ox} (black), fits to data (red), and deconvolution of carbon (blue) and iron (green) waves. The discrepancy between the data and fits, as displayed in the second shell peak of the Fourier transform, displays the inadequacy of the fitting approach for the type 1 initial fit models.

fit. Thus, an excellent fit with reasonable R and σ^2 values could be obtained by using these 3 paths, but only for initial Fe−Fe separations between 2.80 and 3.25 Å.

Type 3 Fits. When all 4 paths were combined to fit the data, excellent fits resulted if only the fit error was taken into account. Closer inspection of the R and σ^2 values revealed either coalescing waves, an unrealistic σ^2 value for **PathC^s**, or an unrealistically short R value for **PathFe**. Therefore, all of these fits were disregarded as possible good fits, but they lend credibility to previous statements about which paths should be included to provide a good fit.

B. Paths Calculated from Synthetic Model Complexes. Fits to the EXAFS data of H_{ox} using phase and amplitude functions calculated from small, synthetic model complexes,[23−32] without modifying their structures, are compiled in Table 2. The fitting protocol developed from the protein crystal structure variations was again used. Three types of fits (type 1, type 2, and type 3) were tested for each model, with paths chosen to approximate the scattering expected

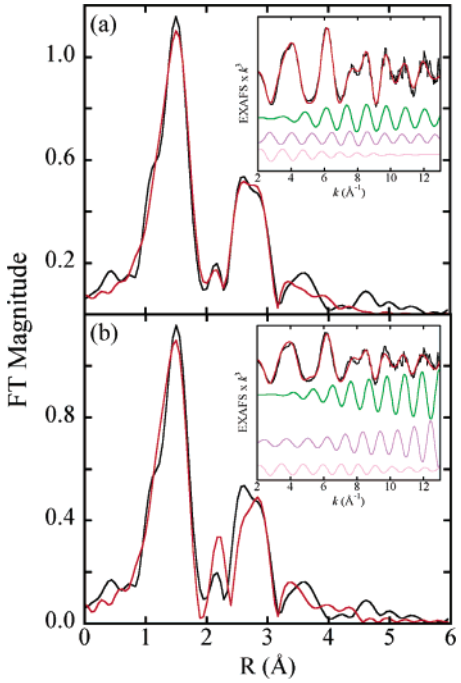

Figure 4. Nonphase shift corrected Fourier transforms (black) and fits of type 2 to the data (red) for H_{ox} with initial Fe−Fe separations from protein crystal structure variations of (a) 2.80−3.25 Å and (b) 3.30−3.50 Å. Insets show EXAFS data of H_{ox} (black), fits to data (red), and deconvolution of iron (green), carbon/oxygen (purple), and carbon/oxygen−nitrogen/carbon multiple scattering (pink) waves. The fitting approach in part a is clearly superior to that in part b.

from the protein crystal structure (C at ∼3.0 Å (**MPathC^s**), Fe (**MPathFe**), C at ∼3.4 Å (**MPathC$^l_{ss}$**), and Fe−N−C multiple scattering at ∼3.5 Å (**MPathC$^l_{ms}$**)). It was evident from inspection of the crystal structures that there were no backscatterers in the range 2.26−2.91 Å, and thus no appropriate path to model the longer first shell (∼2.5 Å) contributions found in the previous fitting process. Therefore, only 1 first shell path and 1 long (∼4.3 Å) multiple scattering path were included in each fit, in addition to the paths listed in Table 2. In all fits that did not result in negative σ^2 values, the first shell fit to a distance of 2.0 Å. The σ^2 value for this path consistently fit to a value similar to that in the protein crystal structure fits. The long-distance multiple scattering path fit to a slightly higher σ^2 value in general, but to a very similar distance when compared to the protein crystal structure fits.

Type 1 Fits. Three classes resulted from type 1 fits, which included scattering from **MPathC^s** and **MPathFe**. For initial Fe−Fe separations between 2.90 and 3.15 Å, two possible fits emerged. Both fits had **MPathC^s** and **MPathFe** competing against each other, with one path fitting to ∼2.9 Å and the other fitting to ∼3.0 Å. In either case, the path that fit to ∼2.9 Å had a very high σ^2 value and therefore contributed little to the overall fit. As can be seen in Figure 5a,b, neither fit provided a good match to the second shell in the Fourier transform, and it is evident that additional intensity is needed to fit the high R side of the Fourier transform peak.

Reasonable R and σ^2 values resulted from the fits of type 1 with initial Fe−Fe separations between 3.20 and 3.53 Å. **MPathC^s** and **MPathFe** fit to 3.03 and 3.36 Å, respectively.

Table 2. Results of Second Shell Fits[a] to H_{ox} Using Synthetic Model Complexes as Input Models

	type 1[b]				type 2[b]				type 3[b]			
	R (Å)	σ^2 (Å^2)	ΔE_0	F[c]	*R* (Å)	σ^2 (Å^2)	ΔE_0	F[c]	*R* (Å)	σ^2 (Å^2)	ΔE_0	F[c]
initial Fe−Fe (Å)		2.94, 3.15[d]				2.94−3.15[d]				2.94, 3.15, 3.53[d]		
4C	3.05	0.0006	−5.87	0.43			−7.94	0.29	3.02	0.0003	−7.64	0.28
1Fe	2.92	0.0141			3.01	0.0037			3.20	0.0112		
4C					3.37	0.0039			3.38	0.0012		
4C−N					3.53	0.0030			3.34	0.0122		
initial Fe−Fe (Å)		3.04, 3.10[d]				3.20−3.53[e]				3.04, 3.10[d]		
4C	2.92	0.0138	−1.74	0.43					2.87	0.0145	−6.00	0.36
1Fe	3.02	0.0029							3.00	0.0035		
4C									3.35	0.0025		
4C−N									3.61	0.0119		
initial Fe−Fe (Å)		3.20−3.31, 3.40−3.53[d]								3.25, 3.40, 3.44[d]		
4C	3.03	0.0014	−6.88	0.36					3.03	0.0001	−6.15	0.27
1Fe	3.36	0.0055							3.19	0.0116		
4C									3.39	0.0011		
4C−N									3.37	0.0094		

[a] Each fit also included 1 first shell O/N path (at 2.0 Å) and 1 long-distance multiple scattering path (at ∼4.3 Å) to complete the fit. [b] Fits of type 1 included contributions from C ∼3.0 Å from Fe (**MPathC^s**) and Fe (**MPathFe**). Fits of type 2 included contributions from C/O ∼3.4 Å from Fe (**MPathC$^l_{ss}$**), the corresponding multiple scattering (**MPathC$^l_{ms}$**), and Fe (**MPathFe**). Fits of type 3 included all 4 paths (**MPathC^s**, **MPathFe**, **MPathC$^l_{ss}$**, and **MPathC$^l_{ms}$**). [c] Error (F) is defined as $F = \sum[[(\chi_{obsd} - \chi_{calcd})^2 k^6]/n]$ where n is the number of data points. [d] Each starting distance provided fits that, within error, could be grouped together. The fit values shown are from one fit but are representative of all fits of that group. [e] Variety of fits all with negative σ^2 values on one or more paths.

Inspection of the fit quality (Figure 5c) indicates that the second shell peak is not well fit, however, because the intensity ratio between the low and high *R* sides of the peak is reversed. This result suggests that the C and Fe waves interact to fit to inappropriate distances.

Type 2 Fits. The majority of type 2 fits (which included **MPathFe**, **MPathC$^1_{ss}$**, and **MPathC$^1_{ms}$**) resulted in negative σ^2 values for at least one path. Included were all fits with initial Fe−Fe separations between 3.2 and 3.5 Å. Good fits were achieved with reasonably low errors for a very small class of fits with initial Fe−Fe separations of 2.94−3.15 Å. **MPathFe** fit to a distance of 3.01 Å, whereas **MPathC$^1_{ss}$** and **MPathC$^1_{ms}$** fit to 3.37 and 3.53 Å, respectively. As can be seen in Figure 6, the fit to the second shell peak is better, but a small amount of intensity is missing from between the first and second shell peaks. This area was fit by the longer first-shell scatterers when the protein crystal structure was used as an initial model, but as previously mentioned, these scatterers are absent in the synthetic models. Therefore, this part of the Fourier transform could not be effectively modeled. Although the errors for this class of type 2 fits are reasonable, they were not as low as the best fits using the protein crystal structure as a model.

Type 3 Fits. As before, all type 3 fits resulted in unrealistic *R* or σ^2 values. **MPathC^s** and **MPathFe** again were highly correlated, with one path having a very high σ^2 value. Once the initial Fe−Fe separation was 3.15 Å or longer, **MPathFe** fit to a variety of distances between 2.5 and 3.6 Å, but always with a very high σ^2 value. In most cases, **MPathC^s** fit to ∼3.0 Å with an unrealistically low or negative σ^2 value.

C. Comparison of the Two Fitting Methods. In order to ensure both the best fit to the data and an unambiguous determination of the Fe−Fe separation in H_{ox}, a systematic fitting approach was developed and applied. Two methods of initial modeling were employed, one using a protein crystal structure and the other using model complex structures. Backscattering from light atoms surrounding the diiron

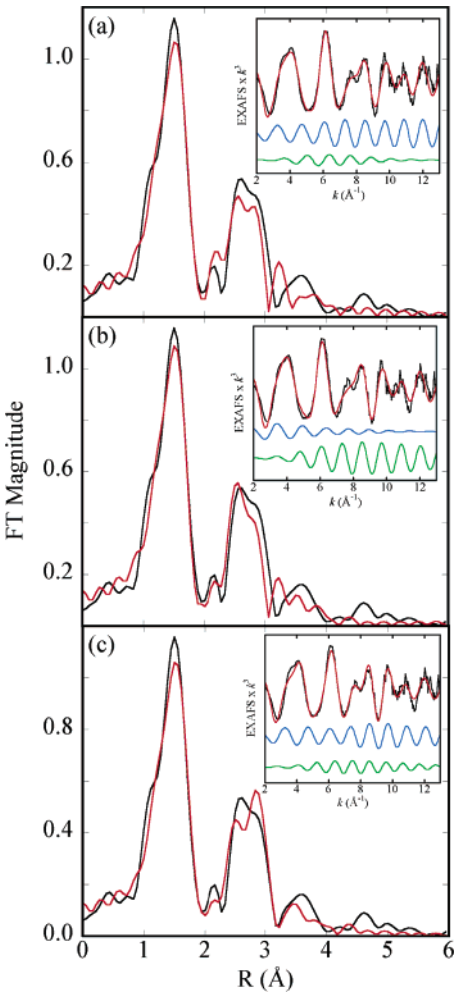

Figure 5. Nonphase shift corrected Fourier transforms (black) and fits of type 1 to the data (red) for H_{ox} with initial Fe−Fe separations from synthetic model complexes of (a) 2.94, 3.15 Å, (b) 3.04, 3.10 Å, and (c) 3.20−3.31, 3.40−3.53 Å. Insets show EXAFS data of H_{ox} (black), fits to data (red), and deconvolution of carbon (blue) and iron (green) waves. None of these fitting approaches provide as good a fit to the data as when a protein crystal structure based initial model is used.

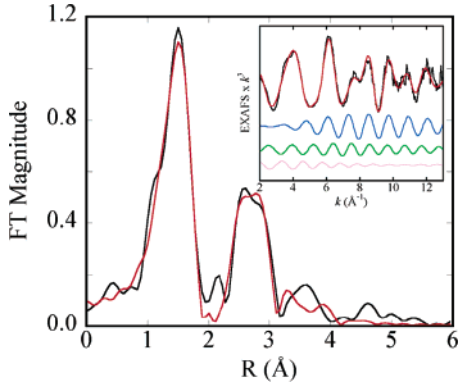

Figure 6. Nonphase shift corrected Fourier transform (black) and fit of type 2 to the data (red) for H_{ox} with initial Fe−Fe separations from synthetic model complexes of 2.94−3.15 Å. Inset shows EXAFS data of H_{ox} (black), fit to data (red), and deconvolution of iron (blue), carbon (green), and carbon−nitrogen multiple scattering (pink) waves. Note that the area of the Fourier transform in the range 1.9−2.3 Å is not well fit by this approach.

center and backscattering between the two Fe atoms were delineated in the study, which also probed whether model bias plays a role in the separation of those waves. Model bias in this study is defined as the influence the initial structure, from which the phase and amplitude functions are calculated, exerts on the final fit parameters, in particular the Fe−Fe distance. Ideally, irrespective of the initial Fe−Fe distance, the same final Fe−Fe separation will be found after the fitting procedure. As described above, however, the final Fe−Fe separation depends on the initial input value, but this model bias could be eliminated by careful examination of all fits. Only initial models that allowed the final Fe−Fe separation to fit to ∼3.0 Å provided the best agreement with the experimental data.

As expected, the scattering from the carbon atoms at ∼3.0 Å from the Fe centers interacted strongly with the scattering between the two Fe atoms. To evaluate this interaction, the Fe−Fe separation was systematically stepped from 2.80 to 3.50 Å, and different combinations of scattering paths were fit to the EXAFS data. The Fe−C wave (represented by **PathC**^{s}) was not able to be separated from the Fe−Fe wave (represented by **PathFe**), and only the Fe−Fe wave was needed to provide a reasonable fit to the data. A C-only fit resulted in an unreasonably low σ^2 value for the C scattering path and poor fits to the second shell peak in the Fourier transform. This result does not imply that there were no carbon scattering contributions in the active site of H_{ox} at ∼3.0 Å, but instead that the total scattering signal is dominated by that of the Fe atom at a very similar distance.

This conclusion was further tested by employing small, synthetic model complexes as the input structures for the calculation of the scattering functions. Inspection of the fit quality and fit errors reveals that the protein crystal structure input functions afforded significantly better fits than those based on the synthetic inorganic complexes. It has already been mentioned that the absence of backscatterers between 2.26 and 2.91 Å in the synthetic models contributed to, but was not the sole reason for, the poorer fits. The synthetic complexes are generally more rigid than the protein active site. Eight out of eleven complexes contain an oxo-bridge with at least one other oxygen-type bridge ligated to iron. Oxo-bridges tend to form short bonds to Fe(III),[23,26,29] and in the eight complexes with the μ-oxo motif, the shortest Fe−O bond ranged from 1.78 to 1.90 Å. Since the pre-edge data establish the absence of such a bridge in the site (vide infra), the paths corresponding to these short Fe−O bonds were not used to fit the first shell scattering in H_{ox}. Instead, the next nearest scatterer to Fe (1.91−2.05 Å) was used to model the first shell bonding. Nevertheless, a test was performed to determine whether the short Fe−O path could model the first shell scattering of H_{ox} effectively. The resulting fits were quite similar to those using the longer first-shell paths in fit parameters and error (fits not shown). In addition to stronger bridges, all synthetic complexes used contain tri- or tetradentate N/O ligation. This type of large, synthetic ligand provides very different scattering functions than the histidine, glutamate, and water ligation present in the H_{ox} active site. This difference accounts for the slightly higher σ^2 values for the fits when the model complexes were used. Moreover, the model bias that was evident in fits using the protein crystal structure as an initial model was again seen in this series of fits, and a smaller range of initial Fe−Fe separations resulted in a final Fe−Fe distance of ∼3.0 Å. Again, using several different initial structural models, and careful examination of the fits, leads to the conclusion that the Fe−Fe separation in H_{ox} is ∼3.0 Å.

Despite the differences between the paths calculated from the protein crystal structure and those calculated from the synthetic model complex structures, within error the same overall best fit was achieved for both methods. This finding strengthens the conclusion that the distance between the two Fe atoms in H_{ox} is 3.0 Å. In both methods, an extensive model bias was observed, and this bias was heightened when the synthetic complexes were used to calculate the scattering paths. This result demonstrates the need for several starting input structures, whether they are variations on a known crystal structure or several model complexes with different metal−metal separations and ligations. Irrespective of the starting structure, a systematic and thorough analysis can unambiguously determine the distances to critical atoms.

D. XAS Comparison of H_{ox} and H_{ox} + MMOD. An overlay of the Fe K-edge spectra of H_{ox} and H_{ox} + MMOD, along with those of two model complexes, is presented in Figure 7. The model complexes are $[Fe_2(\mu\text{-}O)(OAc)_2(HB(pz)_3)_2]$ and $[Fe_2(\mu\text{-}OH)(OAc)_2(HB(pz)_3)_2]^+$, which contain an oxo-bridge and a hydroxo-bridge, respectively, in addition to two acetate bridges. As can be seen in the inset of Figure 7, the 1s → 3d pre-edge transition area for the oxo-bridged species is remarkably different in shape and much more intense than that for the hydroxo-bridged species. The significantly shorter Fe−O_{oxo} bond creates a pseudo-C_{4v} coordination environment for the oxo-bridged complex. This stereochemistry increases the amount of 4p mixing into the 3d orbitals of the Fe center and results in a more intense 1s → 3d pre-edge feature.[34] Fits to the pre-edge region of $[Fe_2(\mu\text{-}O)(OAc)_2(HB(pz)_3)_2]$ revealed two transitions at 7112.7 and 7114.4 eV, with the higher energy feature having 12.5

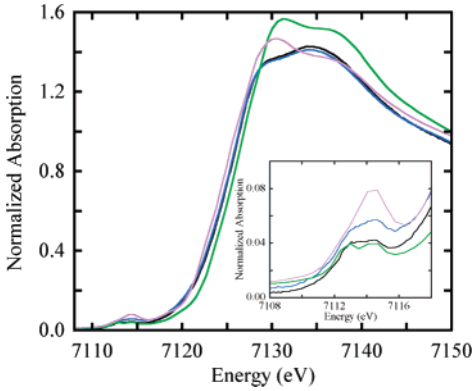

Figure 7. Fe K-edge data for $[Fe_2(\mu\text{-O})(OAc)_2(HB(pz)_3)_2]$ (purple), $[Fe_2(\mu\text{-OH})(OAc)_2(HB(pz)_3)_2]^+$ (green), H_{ox} (black), and H_{ox} + MMOD (blue). Inset shows magnification of 1s → 3d pre-edge transition area.

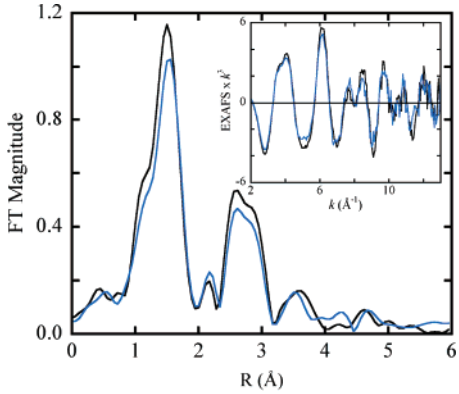

Figure 8. Nonphase shift corrected Fourier transforms (and EXAFS data, inset) for H_{ox}, with (blue) and without (black) MMOD.

Table 3. XAS Pre-Edge Energies and Intensities for $[Fe_2(\mu\text{-O})(OAc)_2(HB(pz)_3)_2]$, $[Fe_2(\mu\text{-OH})(OAc)_2(HB(pz)_3)_2]^+$, H_{ox}, and H_{ox} + MMOD

sample	pre-edge peak energy	pre-edge peak intensity	total pre-edge peak intensity[a]
$[Fe_2(\mu\text{-O})(OAc)_2(HB(pz)_3)_2]$[b]	7112.68(0.05)	4.1(0.5)	16.6(0.7)
	7114.35(0.01)	12.5(1.1)	
$[Fe_2(\mu\text{-OH})(OAc)_2(HB(pz)_3)_2]^+$[b]	7112.68(<0.01)	3.2(0.2)	5.5(0.4)
	7114.35(0.01)	2.3(0.2)	
H_{ox}	7113.12(0.04)	7.0(1.2)	8.1(1.3)
	7114.62(0.06)	1.1(0.1)	
H_{ox} + MMOD	7113.13(0.03)	7.5(0.3)	9.5(0.9)
	7114.59(0.01)	2.1(0.7)	

[a] Values reported for the pre-edge intensity are multiplied by 100 for convenience. [b] Fits previously reported in ref 34.

units of intensity and the lower energy shoulder having 4.1 units of intensity, for a total intensity of 16.6 units (Table 3). This total intensity is typical for oxo-bridged diiron(III) complexes.[34] Fits to the pre-edge region of $[Fe_2(\mu\text{-OH})(OAc)_2(HB(pz)_3)_2]^+$ showed transitions at energy values nearly identical to the oxo-bridged complex, but the intensity of the higher energy transition was much lower (2.3 units), whereas the lower energy transition had about the same value (3.2 units). Analogous fits to the pre-edge region of H_{ox} revealed two transitions shifted to slightly higher energies (7113.1 and 7114.6 eV) from the model complexes with intensities of 7.0 and of 1.1 units, respectively. Two transitions were also identified in the pre-edge of H_{ox} + MMOD at 7113.1 and 7114.6 eV with intensities of 7.5 and 2.1, respectively. All pre-edge fitting results with standard deviations are given in Table 3. Comparison to other previously analyzed diiron(III) complexes suggests that the pre-edges of H_{ox} and H_{ox} + MMOD have intensities similar to those of compounds containing 2 μ-hydroxo bridges or 2 μ-phenolato bridges.[34] A search of the Cambridge Structural Database[22] for diiron(III) complexes resembling the active site of H_{ox} and having Fe−Fe separations in the range 3.0−3.1 Å was performed. This search revealed that several different types of bridges can result in very similar Fe−Fe separations, predominantly a combination of μ-oxo, μ-hydroxo, and μ-acetato bridges. The majority (13 out of 18) of the complexes with this Fe−Fe separation contained one μ-oxo bridge and two other bridges (μ-acetato or μ-benzoato); however, three of the remaining five complexes contained two μ-hydroxo bridges. It would be expected that, although no such structure was found among the synthetic complexes, a similar Fe−Fe distance could be achieved from the combination of a μ-hydroxo, a μ-aqua, and a bidentate bridge. From the EXAFS analysis and the intensity of the pre-edge, it can be stated that neither H_{ox} nor H_{ox} + MMOD contains a short Fe−O, oxo-bridged motif that predominates in the synthetic complexes. It can also be stated that, because the pre-edge regions of H_{ox} with and without MMOD present are nearly identical, and since neither spectrum shows any indication of a significant amount of an oxo-bridged species, a negligible amount of H_{ox} + MMOD contains the short Fe−O distance, oxo-bridged motif that was detected in a small fraction of the sample by optical spectroscopy.[16]

Figure 8 shows an overlay of the Fourier transforms and EXAFS data (inset) of H_{ox} and H_{ox} + MMOD. Like the edge regions of the two samples, there are only very minor differences in these spectra. The EXAFS fitting methodology developed in the previous sections was applied to compare H_{ox} and H_{ox} + MMOD. The same 15 variations using the protein crystal structure and 3 different fit types described above to fit the H_{ox} data were used to fit the H_{ox} + MMOD data set (Table 4). A comparison of the values in Tables 1 and 4 reveals that almost identical fit results were achieved for H_{ox} and H_{ox} + MMOD. The best fit to H_{ox} + MMOD was a type 2 fit, where the initial Fe−Fe separation was between 2.85 and 3.20 Å, and the final Fe−Fe distance was 3.03 Å. The σ^2 values are slightly higher in the best fit to H_{ox} + MMOD than in that for H_{ox}, but the R and fit function values are the same within error for the two samples. Both the higher σ^2 values and smaller acceptable initial Fe−Fe separation range may be due to the slightly poorer data quality in H_{ox} + MMOD as compared to H_{ox}. The best fits for H_{ox} and H_{ox} + MMOD are shown in Figure 9a,b, respectively, and the values for these fits are given in Table 5.

Given the results of this EXAFS analysis and the absence of any feature in the pre-edge region that would suggest a bridging mode change in the active site, we conclude that there is negligible effect observable by XAS at the diiron site of H_{ox} when MMOD is present. Similar results were found in an early XAS study of the interaction between MMOB and the mixed-valent and reduced forms of MMOH.[7]

Table 4. Results of Second Shell Fits[a] to H_{ox} + MMOD Using Protein Crystal Structure Variations as Input Models

	type 1				type 2				type 3			
	R (Å)	σ^2 (Å^2)	ΔE_0	F^b	R (Å)	σ^2 (Å^2)	ΔE_0	F^b	R (Å)	σ^2 (Å^2)	ΔE_0	F^b
initial Fe−Fe (Å)		2.80−2.90, 3.15[c]				2.85−3.20[c]				*d*		
4C	3.05	0.0005	0.04	0.31			−1.24	0.22				
1Fe	2.91	0.0141			3.03	0.0042						
4C/O					3.40	0.0067						
4C/O−N/C					3.55	0.0132						
initial Fe−Fe (Å)		2.95−3.10[c]				3.25−3.45[c]						
4C	3.35	0.1262	0.42	0.26			−4.24	0.28				
1Fe	3.03	0.0037			3.31	−0.0025						
4C/O					3.43	−0.0037						
4C/O−N/C					3.45	−0.0060						
initial Fe−Fe (Å)		3.20−3.45[c]										
4C	3.05	0.0013	−1.00	0.28								
1Fe	3.41	0.0103										
4C/O												
4C/O−N/C												

[a] Each fit also included 2 first shell O/N paths (at 2.01 and 2.45 Å) and 1 long multiple scattering path (at 4.36 Å) to complete the fit. [b] Error (F) is defined as $F = \sum[[(\chi_{obsd} - \chi_{calcd})^2 k^6]/n]$ where n is the number of data points. [c] Each starting distance provided fits that, within error, could be grouped together. The fit values shown are from one fit but are representative of all fits of that group. [d] Variety of fits all with negative or unrealistic σ^2 or R values on one or more paths.

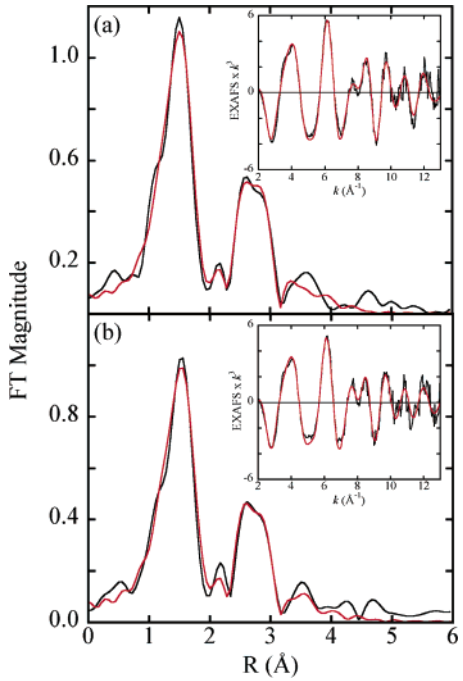

Figure 9. Nonphase shift corrected Fourier transform (black) and best fit to the data (red) for (a) H_{ox} and (b) H_{ox} + MMOD. Inset shows EXAFS data (black) and best fit to the data (red).

Table 5. Final EXAFS Fit Results for H_{ox} and H_{ox} + MMOD

	H_{ox}				H_{ox} + MMOD			
	R (Å)	σ^2 (Å^2)	ΔE_0	F^a	R (Å)	σ^2 (Å^2)	ΔE_0	F^a
5Fe−O/N	1.99	0.0104	−1.82	0.22	2.01	0.0117	−1.24	0.22
1Fe−O	2.45	0.0053			2.45	0.0057		
1Fe−Fe	3.03	0.0033			3.03	0.0042		
4Fe−C/O	3.40	0.0038			3.40	0.0067		
4Fe−N/C−C/O	3.56	0.0051			3.55	0.0132		
5Fe−N−C	4.32	0.0102			4.36	0.0128		

[a] Error (F) is defined as $F = \sum[[(\chi_{obsd} - \chi_{calcd})^2 k^6]/n]$ where n is the number.

Although EPR spectra of MMOH were perturbed in the presence of MMOB, only minor changes at high k were seen in the EXAFS data, which had minimal impacts in fit results using methodology available at the time. It was concluded that the presence of MMOB may have some influence on the electronic structure of the diiron site in MMOH, but no significant structural impact.

Conclusions

Through the development and application of a systematic EXAFS fitting methodology based on ab initio phase and amplitude calculation methods, it is possible to state with high confidence that the Fe−Fe separation in the oxidized form of MMO hydroxylase in solution is 3.0 Å, and not a longer distance as previously thought. The fitting procedure demonstrates the need for the definition and utilization of several initial structures from which phase and amplitude functions are calculated. This procedure avoids input model bias, which can lead to both incorrect or poor fits, and ensures that critical distances are determined unambiguously. We have also shown that small synthetic complexes can provide good starting models, even if used unchanged, in determining the structure of a dinuclear center when employed to calculate the functions. Caution must be used with this method of fitting, however, since the fixed model complex parameters are considerably different from those calculated for a protein input structure. Therefore, synthetic complexes should be used only as a starting point for fitting, and a more appropriate modified model should be constructed from the information gained from the initial fits.

This methodology was instrumental in providing confidence in the comparison between H_{ox} and H_{ox} + MMOD, because the changes to H_{ox} were expected to be small in the presence of MMOD. The analysis revealed no changes to the active site of H_{ox} when MMOD is added, and there is no evidence in either the pre-edge or EXAFS data for a short Fe−O oxo-bridge between the two Fe centers in H_{ox} or H_{ox} + MMOD.

This study provides a foundation for continued investigation of other component and substrate interactions with MMOH, such as the comparison between H_{red} and H_{red} + MMOD, and MMOH interactions with MMOR or MMOB,

and for the structural study of intermediates, like the high-valent intermediate $MMOH_Q$.

Acknowledgment. This work was supported by National Institutes of Health Grants GM32134 (S.J.L.) and RR-01209 (K.O.H.). XAS data were measured at SSRL which is supported by the Department of Energy, Office of Basic Energy Sciences. The Structural Molecular Biology program at SSRL is funded by the National Institutes of Health, National Center for Research Resources, Biomedical Technology Program, and the Department of Energy, Office of Biological and Environmental Research.

IC049716B